

Quantum-Enhanced Processing with Tensor-Network Frontends for Privacy-Aware Federated Medical Diagnosis

Hiroshi Yamauchi
SoftBank Corp.

hiroshi.yamauchi@g.softbank.co.jp

Anders Peter Kragh Dalskov
Partisia

anderspkd@partisia.com

Hideaki Kawaguchi
Keio University

hikawaguchi@keio.jp

Rodney Van Meter
Keio University

rdv@sfc.wide.ad.jp

Abstract—We propose a privacy-aware hybrid framework for federated medical image classification that combines tensor-network representation learning, MPC-secured aggregation, and post-aggregation quantum refinement. The framework is motivated by two practical constraints in privacy-aware federated learning: MPC can introduce substantial communication overhead, and direct quantum processing of high-dimensional medical images is unrealistic with a small number of qubits. To address both constraints within a single architecture, client-side tensor-network frontends, Matrix Product State (MPS), Tree Tensor Network (TTN), and Multi-scale Entanglement Renormalization Ansatz (MERA), compress local inputs into compact latent representations, after which a Quantum-Enhanced Processor (QEP) refines the aggregated latent feature through quantum-state embedding and observable-based readout. Experiments on PneumoniaMNIST show that the effect of the QEP is frontend-dependent rather than uniform across architectures. In the present setting, the TTN+QEP combination exhibits the most balanced overall profile. The results also suggest that the QEP behaves more stably when the qubit count is sufficiently matched to the latent dimension, while noisy conditions degrade performance relative to the noiseless setting. The MPC benchmark further shows that communication cost is governed primarily by the dimension of the protected latent representation. This indicates that tensor-network compression plays a dual role: it enables small-qubit quantum processing on compressed latent features and reduces the communication overhead associated with secure aggregation. Taken together, these results support a co-design perspective in which representation compression, post-aggregation quantum refinement, and privacy-aware deployment should be optimized jointly.

Index Terms—Federated Learning, Secure Aggregation, Multi-Party Computation, Tensor Networks, Quantum-Classical Hybrid Machine Learning, Privacy-Aware Learning

I. INTRODUCTION

The rapid digitalization of healthcare, finance, and public infrastructure has led to a sustained increase in distributed, privacy-sensitive data. In medical domains in particular, electronic health records, imaging repositories, and wearable sensor streams are inherently decentralized across hospitals and institutions [1], [2]. At the same time, regulatory frameworks such as the General Data Protection Regulation (GDPR) [3], the Health Insurance Portability and Accountability Act (HIPAA) [4], and national medical data protection laws including Japan’s Act on the Protection of Personal Information (APPI) [5] and the Next-Generation Medical

Infrastructure Act [6] impose strict restrictions on data centralization and cross-institutional sharing. Recent policy initiatives such as the European Health Data Space (EHDS) [7] further reinforce the need for controlled secondary use of medical data under strong governance requirements. As a result, modern medical AI faces a central tension: high-performance learning benefits from access to broad and heterogeneous data, whereas direct data pooling is increasingly constrained.

Federated learning (FL) has therefore emerged as an important paradigm for privacy-sensitive collaborative learning because it allows multiple institutions to participate in joint model training without transferring raw data to a central repository [8], [9]. This setting is especially relevant in medicine, where data locality is often a regulatory and operational requirement rather than a design preference [1]. However, data locality alone does not fully resolve the privacy problem. Even when raw inputs remain on site, gradients, intermediate representations, and model updates can still leak sensitive information through inversion and inference attacks [10], [11]. Because such attacks rely on access to individual client updates, restricting visibility to aggregated information becomes an important design principle.

Secure aggregation based on multi-party computation (MPC) mitigates this risk by ensuring that only aggregated client contributions become available [12]. In MPC, a value is decomposed into secret shares distributed across separate non-colluding computation nodes, which jointly execute a protocol on protected inputs. The final output is reconstructed only from the shares, while no party learns more than what is implied by the released result. MPC is therefore a natural choice for protecting client contributions. Moreover, because this work investigates a constructive use of quantum computation, it is also necessary to consider the possibility that quantum computation could be exploited by a malicious adversary to compromise privacy. The privacy mechanism should therefore remain secure against quantum-computer-aided attackers. Secret-sharing-based MPC, including the variant considered in this work, provides unconditional security. Accordingly, the MPC model adopted here is secure against *any* computational adversary, including quantum-computational ones.

While privacy in the present framework is provided by MPC-secured aggregation, an additional security question

arises if the post-aggregation Quantum-Enhanced Processor (QEP) is delegated to an external quantum server. Blind quantum computing (BQC), including enclave-based approaches such as QEnclave, offers a possible way to hide such delegated quantum computations from the server [13], [14], [15], but this lies outside the present scope.

Although MPC strengthens privacy protection, it also introduces a nontrivial systems trade-off. Expanding the protected portion of the pipeline, or adopting stronger adversarial assumptions, generally increases communication and execution overhead. This raises a fundamental architectural question for regulated federated learning: how should privacy strength, representation dimension, and downstream inference quality be balanced within a single system? The question becomes even more consequential when quantum enhancement is introduced, because any quantum module must operate under the constraints imposed by secure aggregation while remaining compatible with the structure of the aggregated latent representation.

In parallel, hybrid quantum machine learning has attracted attention as a framework for structured nonlinear feature transformation. Distributed quantum neural network models [16], communication-efficient quantum learning algorithms [17], and broader studies of distributed quantum computing and simulation [18], [19] suggest that quantum-enhanced learning should be evaluated together with systems-level scalability considerations. Hybrid tensor-network and quantum-classical models [20], [21], [22], [23], [24], [25] further suggest that structured classical representations can serve as effective interfaces to downstream quantum feature-processing modules. In privacy-preserving quantum federated settings, Li *et al.* proposed quantum-native federated protocols based on gradient hiding and private inner-product estimation [26]. Nevertheless, prior studies have typically emphasized either protocol design or hybrid model design in isolation, and they do not sufficiently characterize how a post-aggregation quantum refinement module behaves when embedded in a privacy-aware federated learning pipeline that simultaneously includes representation compression and secure aggregation.

A further challenge arises from current hardware limitations. Available quantum processors provide only a limited number of usable qubits, so directly processing large medical-image inputs within a quantum module is generally unrealistic. In practice, a useful hybrid design must make effective use of a small quantum system rather than assume access to large fault-tolerant devices. This requires a representation strategy that compresses the original input before quantum processing while preserving task-relevant information.

Tensor networks (TNs) are a natural candidate for this role. Matrix Product States (MPS) were introduced as expressive supervised learning models in [27], and subsequent work explored spectral tensor-train parameterizations [28], residual tensor-train architectures [29], and MPS pre-training strategies for quantum learning [30]. Tensor networks have also been applied to generative modeling [31], high-energy physics event reconstruction [32], and sequential state learning [33].

Recent work has additionally examined TNs in federated and distributed settings, including coupled tensor-train decomposition for federated learning [34] and hierarchical tensor-network-based federated frameworks [35]. Collectively, these studies establish TNs as compact alternatives to dense neural architectures with explicit structural inductive bias. In the present setting, their role is twofold. First, they compress large client-side inputs into low-dimensional latent representations, making post-aggregation quantum processing feasible with a small number of qubits. Second, because the protected representation itself becomes smaller, they reduce the communication overhead incurred by MPC on that representation.

Despite these promising ingredients, prior work has not sufficiently integrated them within a single privacy-aware federated learning pipeline. Two questions remain particularly unresolved: whether compressed latent representations can simultaneously improve the practicality of MPC and support effective small-qubit quantum processing, and whether the benefit of post-aggregation quantum refinement depends on the tensor-network architecture that produces the latent representation.

These issues motivate the present study. The first unresolved problem is practical: MPC can improve privacy in federated learning, but its communication overhead becomes burdensome when high-dimensional representations must be protected. The second unresolved problem is architectural: if only a small number of qubits is available, then the utility of a quantum module depends critically on how the input is compressed before quantum processing. The third unresolved problem is empirical: it remains unclear whether the effect of post-aggregation quantum enhancement is architecture-independent or instead determined by its interaction with the frontend representation.

To address these issues, we propose an end-to-end privacy-aware federated learning framework for medical image classification that combines client-side tensor-network encoding, MPC-secured aggregation of latent representations, and post-aggregation quantum refinement by a Quantum-Enhanced Processor (QEP). We compare three tensor-network frontends—MPS, TTN, and MERA—and evaluate how the effect of the QEP depends on the latent structure supplied by the frontend. The resulting design is intended to support small-qubit quantum processing while reducing the communication overhead associated with secure aggregation.

Experiments are conducted on PneumoniaMNIST [36], a compact biomedical benchmark suitable for controlled evaluation of privacy-aware federated learning pipelines. Our analysis yields two main findings. First, the effect of the QEP depends on its pairing with the tensor-network frontend rather than on the quantum module alone. In particular, the combination of TTN and QEP shows the most favorable overall profile in the present setting, with the clearest positive tendency under quantum enhancement. By contrast, MPS, TTN, and MERA occupy distinct operating regimes in their internal behavior, indicating that the impact of quantum enhancement is architecture-dependent. Second, the MPC benchmark shows

that communication cost is governed primarily by the dimension of the protected representation. This means that tensor-network compression not only makes small-qubit quantum processing feasible, but also improves the practicality of secure deployment by reducing the communication overhead associated with MPC.

The central premise of this study is therefore that representation compression, secure aggregation, and quantum refinement should not be treated as independent design variables. Compressing the input before aggregation changes the cost of privacy protection; the resulting latent structure conditions the behavior of the quantum module; and the practical value of the overall pipeline depends on balancing predictive performance, quantum operating behavior, and secure-computation cost. From this perspective, the main contribution of this work is not a standalone quantum algorithm, but a co-designed system showing how tensor-network compression can support small-qubit quantum enhancement in privacy-aware federated learning.

To summarize, the main contributions of this work are as follows:

- We present an end-to-end privacy-aware hybrid learning framework that combines tensor-network latent encoding, MPC-secured aggregation, and post-aggregation quantum refinement for federated medical image classification.
- We show that tensor-network compression plays a dual role: it supports small-qubit quantum processing on compressed latent features and simultaneously reduces the communication overhead of MPC-secured aggregation.
- We demonstrate that the effect of the Quantum-Enhanced Processor is architecture-dependent and that, in the present setting, the TTN+QEP combination provides the most favorable overall profile, including improved performance relative to its classical counterpart.

The remainder of this paper is organized as follows. Section II presents the proposed framework, including the tensor-network frontends, the MPC-secured aggregation setting, and the Quantum-Enhanced Processor. Section III describes the dataset, training setup, and evaluation protocol. Section IV defines the experimental analyses. Section V reports the results, Section VI discusses their implications and limitations, and Section VII concludes the paper.

II. METHODOLOGY

Fig. 1 shows the proposed privacy-aware federated learning framework. The architecture consists of three coupled stages: client-side tensor-network encoding, MPC-secured aggregation of latent representations, and post-aggregation refinement by a Quantum-Enhanced Processor (QEP). The framework is formulated as an integrated TN+MPC+QEP pipeline so that representational compression, protected aggregation, and quantum refinement can be analyzed within a unified setting.

At the client side, each local input is transformed into a compact latent representation by a tensor-network frontend. These latent features are then combined through an MPC-secured aggregation layer that produces a protected global

representation, which is subsequently processed by the QEP before final classification. Experiment 1 evaluates the end-to-end predictive behavior of this system under different tensor-network frontends, whereas Experiment 2 isolates the MPC-secured aggregation stage and analyzes its communication cost under progressively stronger security settings.

A. Client-Side Tensor-Network Embedding

Each client branch transforms an input chest X-ray image into a compact latent representation before server-side aggregation. Let

$$x \in \mathbb{R}^{784} \quad (1)$$

denote the flattened 28×28 grayscale image. The client-side embedding is written as

$$f_i = \phi_i(\psi_i(x)), \quad f_i \in \mathbb{R}^d, \quad (2)$$

where $i \in \{1, \dots, n\}$ indexes the client, ψ_i denotes a frontend-dependent preprocessing map, and ϕ_i denotes the tensor-network encoder.

In the implementation, the preprocessing stage depends on the frontend type. For the MPS branch, the flattened input is first passed through a shallow real-valued block,

$$\psi_i^{\text{MPS}} : \mathbb{R}^{784} \rightarrow \mathbb{R}^h, \quad (3)$$

consisting of a linear layer, layer normalization, and ReLU activation. The resulting feature is then partitioned into multiple sites and embedded into a complex-valued Matrix Product State (MPS) encoder with QR-based left-canonical projection.

For the TTN and MERA branches, the input is first reorganized into non-overlapping image patches rather than being directly reshaped as a one-dimensional vector sequence. In particular, the 28×28 image is partitioned into 16 patches of size 7×7 , and each patch is processed by a shared patch-wise stem network:

$$\psi_i^{\text{tree}} : \mathbb{R}^{784} \rightarrow \mathbb{R}^{N_p \times d_p}, \quad (4)$$

where $N_p = 16$ is the number of patches and d_p is the patch feature dimension after the stem transformation. These patch tokens are then mapped into complex local vectors and passed to either a Tree Tensor Network (TTN) or a MERA-style hierarchical encoder.

Accordingly, the client-side tensor-network block serves two roles. First, it compresses the original image into a lower-dimensional latent representation before aggregation, reducing the dimensional burden of the subsequent server-side pipeline. Second, it determines the latent geometry on which the Quantum-Enhanced Processor (QEP) later operates. In this sense, the TN frontend is not merely a compression stage, but the structural interface that conditions downstream quantum refinement.

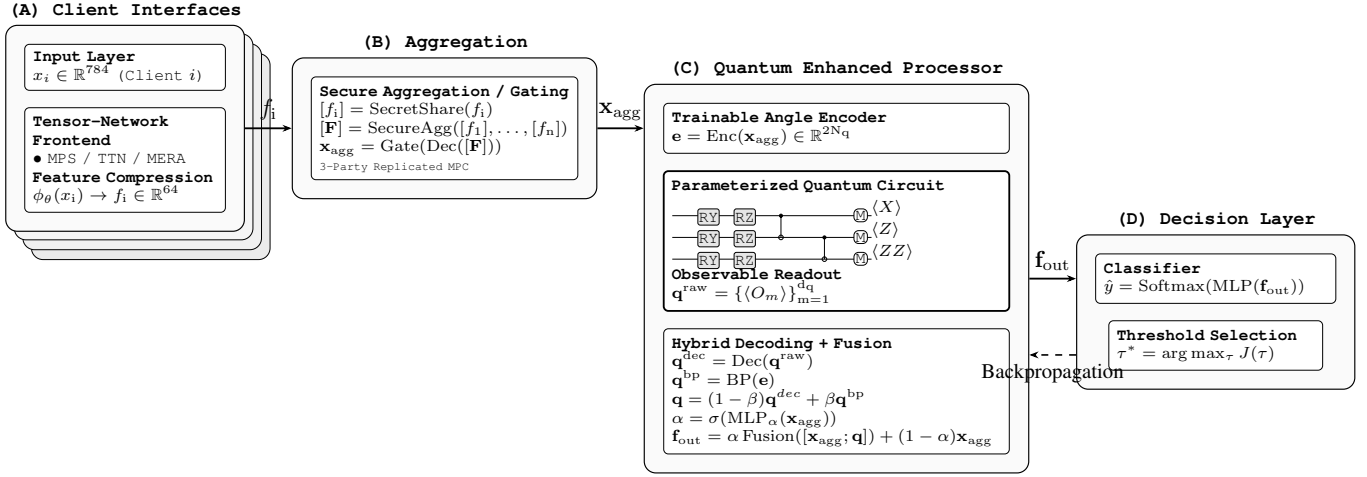


Fig. 1: End-to-end overview of the proposed framework. Client-side tensor-network embedding compresses each local input into a latent representation, MPC-secured aggregation and gating produce a protected global latent feature, and the Quantum-Enhanced Processor (QEP) performs post-aggregation quantum refinement before final decision making. Experiment 1 evaluates the inference performance of this pipeline across different tensor-network frontends, while Experiment 2 analyzes the communication cost of the MPC-secured aggregation component through an abstract protected-aggregation model.

1) *MPS*: For the MPS branch, the preprocessed real-valued feature

$$z = \psi_i^{\text{MPS}}(x) \in \mathbb{R}^h \quad (5)$$

is partitioned into a sequence of L local blocks,

$$z \mapsto \{z^{(1)}, \dots, z^{(L)}\}, \quad z^{(k)} \in \mathbb{R}^{d_{\text{loc}}}, \quad (6)$$

with $h = Ld_{\text{loc}}$. Each local block is then mapped to a complex-valued local vector,

$$\tilde{z}^{(k)} \in \mathbb{C}^{d_{\text{phys}}}, \quad (7)$$

through a learnable complex embedding layer. The MPS is parameterized by a sequence of site-local core tensors. At site k , the core is a third-order tensor

$$A^{(k)} \in \mathbb{C}^{r_k \times d_{\text{phys}} \times r_{k+1}}, \quad (8)$$

where d_{phys} is the local physical dimension and r_k, r_{k+1} are the left and right bond dimensions, respectively.

Starting from an initial boundary state $v^{(0)} \in \mathbb{C}^{r_1}$, the hidden state is updated sequentially as

$$v_\beta^{(k)} = \sum_{\alpha=1}^{r_k} \sum_{s=1}^{d_{\text{phys}}} v_\alpha^{(k-1)} A_{\alpha s \beta}^{(k)} \tilde{z}_s^{(k)}. \quad (9)$$

In the implementation, the site tensors are parameterized in a QR-projected left-canonical form, so that the matricized tensor approximately satisfies

$$(A^{(k)})^\dagger A^{(k)} \approx I. \quad (10)$$

This constraint improves numerical stability during sequential contraction. In addition, the intermediate hidden state is normalized at each step to control norm growth or collapse.

After the final contraction, the resulting complex state is converted to a real-valued feature and projected to the shared latent dimension d .

2) *TTN*: For the TTN branch, the input image is first partitioned into non-overlapping patches and mapped to a sequence of patch features,

$$x \mapsto \{u^{(1)}, \dots, u^{(N_p)}\}, \quad u^{(j)} \in \mathbb{R}^{d_p}, \quad (11)$$

where N_p denotes the number of patches. Each patch feature is then embedded into a complex local vector

$$\tilde{u}^{(j)} \in \mathbb{C}^{d_{\text{loc}}}. \quad (12)$$

The TTN recursively combines neighboring nodes in a binary-tree fashion. Given two child states

$$h_{2j-1}^{(\ell)}, h_{2j}^{(\ell)} \in \mathbb{C}^{d_{\text{loc}}}, \quad (13)$$

their parent state is computed by concatenation followed by an isometric map,

$$h_j^{(\ell+1)} = \mathcal{W}^{(\ell)} [h_{2j-1}^{(\ell)} \parallel h_{2j}^{(\ell)}], \quad \mathcal{W}^{(\ell)} : \mathbb{C}^{2d_{\text{loc}}} \rightarrow \mathbb{C}^{d_{\text{loc}}}, \quad (14)$$

where $[\cdot \parallel \cdot]$ denotes vector concatenation. In the implementation, $\mathcal{W}^{(\ell)}$ is parameterized as a complex isometric transformation obtained through QR-based projection, so that

$$(\mathcal{W}^{(\ell)})^\dagger \mathcal{W}^{(\ell)} \approx I. \quad (15)$$

After each aggregation level, the hidden state is normalized for numerical stability.

After the final contraction, the root state is converted to a real-valued feature and projected to \mathbb{R}^d .

3) *MERA*: The MERA frontend extends the tree-structured aggregation of TTN by interleaving local mixing and coarse-graining across multiple scales. As in the TTN branch, the input image is first represented as a sequence of patch-level local features and embedded into complex local states

$$\tilde{u}^{(j)} \in \mathbb{C}^{d_{\text{loc}}}. \quad (16)$$

At each hierarchical level ℓ , neighboring hidden states are first transformed by disentangling operations. Given two local states

$$h_a^{(\ell)}, h_b^{(\ell)} \in \mathbb{C}^{d_{\text{loc}}}, \quad (17)$$

they are concatenated and mapped by a learned unitary transformation

$$\mathcal{U}^{(\ell)} : \mathbb{C}^{2d_{\text{loc}}} \rightarrow \mathbb{C}^{2d_{\text{loc}}}, \quad (18)$$

followed by a split back into two updated local states. In the implementation, these disentanglers are applied in two stages: first on even pairs $(0, 1), (2, 3), \dots$, and then on odd pairs $(1, 2), (3, 4), \dots$. This alternating pattern changes the local coupling structure across each level without requiring a cyclic shift.

After local mixing, neighboring states are coarse-grained through an isometric map

$$\mathcal{W}^{(\ell)} : \mathbb{C}^{2d_{\text{loc}}} \rightarrow \mathbb{C}^{d_{\text{loc}}}, \quad (19)$$

which produces the hidden states of the next coarser scale,

$$h_j^{(\ell+1)} = \mathcal{W}^{(\ell)} \left[\hat{h}_{2j-1}^{(\ell)} \parallel \hat{h}_{2j}^{(\ell)} \right], \quad (20)$$

where $\hat{h}^{(\ell)}$ denotes the disentangled local states. Both the disentangling and coarse-graining maps are implemented as QR-projected complex transformations, and the hidden states are normalized after each coarse-graining step for numerical stability.

After the final level, the root state is converted to a real-valued latent representation and projected to \mathbb{R}^d . Although the tensor-network frontend is described at the modeling level over real-valued latent features (with complex internal tensor states where appropriate), the discrete fixed-point assumption is introduced only for the MPC benchmark; the effect of explicitly quantizing TN outputs before secure computation is not evaluated in the present study.

B. Security Model and MPC Preliminaries

1) *System Model and Threat Model*: We consider n clients $\{C_i\}_{i=1}^n$ and an aggregation server S . Each client holds a private dataset \mathcal{D}_i and computes a local representation $f_i \in \mathbb{R}^d$. For the MPC cost analysis, we additionally introduce a client-specific scalar coefficient $w_i \in \mathbb{R}$ to model protected weighted aggregation and normalization, as described in Section II-C.

To protect client data, we use an outsourced 3-party MPC model in which the role of S is distributed across three non-colluding computation nodes S_0, S_1, S_2 . We consider both passive and active security. Scenarios 1–3 correspond to passive-security settings, whereas Scenarios 4–6 are their active-security counterparts.

2) *Cost Model*: We model secure aggregation using replicated secret sharing over \mathbb{Z}_{2^k} with three non-colluding computation nodes. Under this model, addition and multiplication by public constants are local, whereas secure multiplication requires communication between nodes. Real-valued computation is handled in fixed-point form, so multiplication

additionally requires truncation, and normalization requires secure division.

In the communication model used in this paper, one secure multiplication costs $3k$ bits, one truncation costs $6k$ bits, and a full fixed-point multiplication therefore costs $9k$ bits. Secure division is modeled with communication cost $3k(k + 4\theta + 2)$, where θ denotes the number of refinement iterations. Active security is modeled by doubling the communication cost. Because our focus is communication benchmarking rather than protocol derivation, we use these established costs directly and do not reproduce the full protocol details here.

C. Secure Aggregation via MPC

The proposed end-to-end framework includes an MPC-secured aggregation stage between client-side tensor-network embedding and post-aggregation quantum refinement. For inference evaluation, this functionality is studied through the system-level architecture shown in Fig. 1. For communication-cost analysis, we abstract the aggregation stage into a protected weighted aggregation form so that its security and communication overhead can be studied independently of low-level implementation details.

Let $f_i \in \mathbb{R}^d$ denote the latent representation produced by client i , and let $w_i \in \mathbb{R}$ denote a client-specific scalar coefficient used in the protected aggregation model. The aggregated weighted feature and total weight are defined as

$$\text{WF} = \sum_{i=1}^n w_i f_i, \quad \text{W} = \sum_{i=1}^n w_i. \quad (21)$$

The normalized aggregate is then written as

$$x = \frac{\text{WF}}{\text{W} + \varepsilon}. \quad (22)$$

The MPC scenarios considered in this work correspond to progressively richer protected functionality within the abstract secure-aggregation model. Scenario 1 protects only the computation of WF and W, and Scenario 2 additionally protects the normalization step that produces x . Scenario 3 further protects the post-normalization feature-transformation stage described in Section II-D. Scenarios 4–6 represent the active-security counterparts of Scenarios 1–3, respectively.

D. Quantum-Enhanced Processor

The central quantum component of the framework is the Quantum-Enhanced Processor (QEP), which refines the aggregated latent representation through a hybrid quantum-classical transformation. Let the aggregated server-side feature be denoted by

$$\mathbf{x}_{\text{agg}} \in \mathbb{R}^d. \quad (23)$$

The QEP maps \mathbf{x}_{agg} to a quantum-derived feature vector through a quantum-state embedding followed by observable-based readout, and fuses it with the original classical representation via adaptive residual mixing. In the present implementation, the quantum circuit is not treated as a trainable component. Instead, it is evaluated using statevector simulation

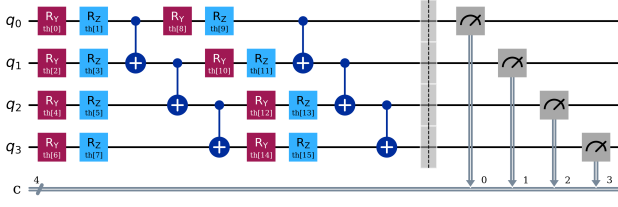


Fig. 2: Parameterized quantum circuit used in the QEP. Each layer applies single-qubit R_y and R_z rotations followed by nearest-neighbor CNOT entangling gates. For visualization, terminal measurement gates are shown explicitly. In the actual implementation, however, the circuit output is summarized through expectation values of selected Pauli observables rather than bitstring sampling.

and used as a fixed nonlinear feature transformation that deterministically maps the input to quantum-derived statistics.

As a result, gradient-based optimization is not applied to the quantum circuit itself. Instead, only the surrounding classical components—including the encoder, decoder, and fusion modules—are trained to determine how the quantum-derived features are incorporated into the latent representation. This design allows the QEP to function as a quantum feature extractor rather than as a variational quantum model.

From a representational viewpoint, the QEP can be interpreted as a feature-expansion mechanism that embeds a compact latent vector into a quantum Hilbert space and extracts observable-based statistics. In this setting, the effective dimensionality of the quantum feature space is determined by the number of observables used for measurement rather than by the number of circuit parameters. To ensure sufficient expressivity, it is therefore desirable that the number of quantum features d_q be comparable to the latent dimension d . When using both one-body and two-body Pauli observables, this leads to a scaling relation $d_q = \mathcal{O}(N_q^2)$, suggesting that the number of qubits should scale approximately as $N_q \sim \sqrt{d}$. This consideration motivates the choice of qubit counts in the present study, and its empirical validity is examined in the qubit-scaling experiments described later.

1) *Quantum Encoding and Observable Readout*: The QEP first applies a trainable angle encoder

$$\mathbf{e} = \text{Enc}(\mathbf{x}_{\text{agg}}), \quad \mathbf{e} \in \mathbb{R}^{2N_q}, \quad (24)$$

where N_q is the number of qubits and $\text{Enc}(\cdot)$ denotes a shallow multilayer perceptron with normalization and nonlinear activation. For each layer l and qubit q , rotation angles are defined as

$$\theta_y^{(l,q)} = \pi s \left(e_{2q-1} + \delta_y^{(l,q)} \right), \quad \theta_z^{(l,q)} = \pi s \left(e_{2q} + \delta_z^{(l,q)} \right), \quad (25)$$

with global scale s and circuit-side angle offsets $\delta_y^{(l,q)}, \delta_z^{(l,q)}$.

Starting from $|0\rangle^{\otimes N_q}$, the circuit applies repeated layers of single-qubit R_y/R_z rotations followed by nearest-neighbor

CNOT gates:

$$U(\mathbf{x}_{\text{agg}}) = \prod_{l=1}^L \left[\left(\prod_{q=1}^{N_q-1} \text{CX}_{q,q+1} \right) \left(\prod_{q=1}^{N_q} R_z \left(\theta_z^{(l,q)} \right) R_y \left(\theta_y^{(l,q)} \right) \right) \right]. \quad (26)$$

For a circuit with N_q qubits and depth L , this construction uses $2LN_q$ single-qubit rotation gates and $L(N_q - 1)$ nearest-neighbor CNOT gates. The final quantum feature dimension is then determined by the selected observable set used for expectation-value evaluation. Fig. 2 illustrates the circuit structure used in the QEP.

The resulting state is summarized through expectation values of Pauli observables. For each observable \hat{O}_m , the corresponding quantum statistic is

$$q_m^{\text{raw}} = \langle \psi(\mathbf{x}_{\text{agg}}) | \hat{O}_m | \psi(\mathbf{x}_{\text{agg}}) \rangle, \quad (27)$$

which yields a raw quantum feature vector

$$\mathbf{q}^{\text{raw}} \in \mathbb{R}^{d_q}, \quad (28)$$

where d_q is determined by the number and type of observables. In practice, this allows the model to extract higher-order correlations and nonlinear features from a compact latent representation without requiring a large quantum register.

2) *Classical Decoding and Residual Fusion*: The raw quantum statistics are first decoded into the latent feature space through a trainable decoder

$$\mathbf{q}^{\text{dec}} = \text{Dec}(\mathbf{q}^{\text{raw}}) \in \mathbb{R}^d. \quad (29)$$

In parallel, the encoded angle vector is passed through a differentiable bypass pathway,

$$\mathbf{q}^{\text{bp}} = \text{BP}(\mathbf{e}) \in \mathbb{R}^d, \quad (30)$$

and the two branches are mixed as

$$\mathbf{q} = (1 - \beta) \mathbf{q}^{\text{dec}} + \beta \mathbf{q}^{\text{bp}}, \quad (31)$$

where $\beta \in (0, 1)$ is a learned scalar gate. This design allows the encoder to remain trainable even though the quantum simulation itself is treated as non-differentiable.

The resulting quantum-enhanced representation is then fused with the original classical feature:

$$\mathbf{z} = \text{Fusion}([\mathbf{x}_{\text{agg}}; \mathbf{q}]). \quad (32)$$

A sample-wise scalar gate

$$\alpha = \sigma(W_\alpha \text{LN}(\mathbf{x}_{\text{agg}}) + b_\alpha) \quad (33)$$

controls the final interpolation

$$\mathbf{f}_{\text{out}} = \alpha \mathbf{z} + (1 - \alpha) \mathbf{x}_{\text{agg}}. \quad (34)$$

In this way, the model can adaptively control the contribution of the quantum-enhanced branch rather than relying on it uniformly across all samples. The QEP is therefore not only a simulated quantum feature map, but also a learned controller over how strongly quantum-derived information influences the final latent representation.

3) *Training Objective*: The final classifier is trained with weighted cross-entropy. In addition, an auxiliary supervision term can be applied to the representation produced by the quantum-enhanced branch:

$$\mathcal{L} = \mathcal{L}_{\text{cls}} + \lambda_q \mathcal{L}_{\text{aux}}, \quad (35)$$

where \mathcal{L}_{aux} encourages the quantum-enhanced pathway to retain task-relevant information. Overall, the QEP should be interpreted as a hybrid feature-refinement module whose contribution depends on how quantum-derived features interact with the latent structure provided by the frontend architecture.

Only the surrounding classical components—including the encoder, decoder, bypass pathway, and fusion modules—are optimized during training, while the quantum circuit serves as a fixed observable-based feature transformation.

III. EXPERIMENTAL SETUP

We evaluated the proposed framework on PneumoniaMNIST, a binary medical image classification benchmark from the MedMNIST collection [36]. The dataset is derived from pediatric chest X-ray images, and the task is to discriminate *Normal* from *Pneumonia*. Following the official preprocessing protocol, each image was resized to 28×28 pixels, yielding a single-channel grayscale input. In the implementation, each image was normalized to the range $[0, 1]$. For the MPS branch, the image was flattened into a 784-dimensional vector. For the TTN and MERA branches, the same image was additionally reorganized into 16 non-overlapping patches of size 7×7 , followed by a shared patch-wise stem transformation. The standard training, validation, and test splits provided by the dataset interface were used throughout the experiments. Fig. 3 shows representative examples of the resized grayscale chest X-ray images in PneumoniaMNIST, including both Normal and Pneumonia cases.

To reflect the distributed setting of the proposed architecture, the data in each split were partitioned across multiple client branches using label-stratified client assignment. Unless otherwise noted, the number of client branches was fixed at 16. Training used a per-client local batch size of 4, yielding up to 64 samples per federated training step when all client branches contributed non-empty batches. This configuration is consistent with the client-side tensor-network embedding pipeline described in Section II-A, where each branch produces a compressed latent representation prior to server-side gating and optional quantum enhancement.

The overall model consisted of three stages: a client-side tensor-network embedding module, a server-side feature-gating module, and a Quantum-Enhanced Processor (QEP), followed by a classical classifier. For the client-side tensor-network interface, we considered three architectures: Matrix Product State (MPS), Tree Tensor Network (TTN), and Multi-scale Entanglement Renormalization Ansatz (MERA). In all cases, the shared latent feature dimension was fixed to 64. The primary goal of the experiments was to characterize how the QEP behaves across these frontend-induced latent structures.

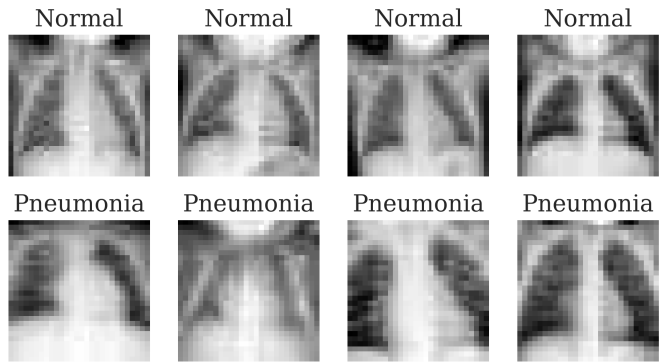


Fig. 3: Example samples from PneumoniaMNIST. The top row shows Normal cases and the bottom row shows Pneumonia cases. All images are resized grayscale chest X-ray images used in the present experiments.

Training was performed for 20 epochs using Adam with parameter-group-specific learning rates and weight decay 10^{-5} . The tensor-network, patch-stem, quantum-encoder-related, and remaining head parameters were optimized with learning rates 1×10^{-5} , 3×10^{-5} , 5×10^{-5} , and 1×10^{-4} , respectively. To account for class imbalance, weighted cross-entropy was used with class weights computed from the training split. In the quantum-enabled setting, the auxiliary supervision term for the quantum-enhanced branch was activated with weight 0.5.

For the QEP, the quantum branch used 16 qubits, circuit depth 2, angle scale 0.5, and refresh interval 1. Quantum expectation values were computed with Qiskit Aer in statevector mode. The circuit consisted of repeated layers of single-qubit R_y and R_z rotations followed by nearest-neighbor CNOT entangling gates, and the observable set included one-body Pauli terms together with selected two-body correlations. The resulting quantum statistics were classically decoded into the shared latent feature space and adaptively fused with the classical pathway.

We report both standard-threshold and threshold-optimized evaluation. In the standard setting, the Pneumonia posterior was thresholded at 0.5. In the optimized setting, the threshold was selected on the validation split from the ROC curve using Youden’s J statistic and then applied to the test split. Performance was assessed using Accuracy, Precision, Recall, and F1-score for both Normal and Pneumonia classes. For quantum runs, we additionally analyzed internal QEP diagnostics, including the mean fusion coefficient α , the standard deviation of the quantum-enhanced branch representation (q -std), the mean magnitude of the quantum feature vector, and the cosine similarity between classical and quantum features, in order to characterize the internal operating regime of the QEP.

We also examined the behavior of the QEP under qubit scaling and noise variation. To study scalability with respect to quantum register size, we varied the number of qubits from 4 to 16 while keeping the remaining training and evaluation

protocol unchanged. To study noise sensitivity, we fixed the QEP to 8 qubits and compared noiseless simulation, depolarizing noise, thermal noise, and a mixed-noise configuration. Because the present QEP is implemented as a simulation-based observable feature generator, these analyses should be interpreted as controlled studies of the operating range and robustness of the quantum branch rather than as hardware-performance claims.

The comparison in this study is intended to evaluate practically instantiated frontend families rather than a strictly topology-isolated control in which all preprocessing components are forced to be identical. Accordingly, each frontend is implemented in a form suited to its own structural bias, and the comparison is used to examine how different tensor-network representation regimes interact with post-aggregation quantum refinement within the same end-to-end framework.

Based on this common training and evaluation setting, we define two complementary experiments: one for end-to-end predictive analysis and one for MPC communication-cost benchmarking.

IV. EXPERIMENTS

A. Experiment 1: Quantum Enhancement across MPS, TTN, and MERA

The first experiment characterizes how the Quantum-Enhanced Processor (QEP) behaves across different client-side tensor-network architectures. Specifically, we compare Classical and Quantum modes for MPS, TTN, and MERA in order to determine whether the contribution of the QEP depends on the latent structure induced by the tensor-network frontend.

In the Classical mode, the server-side feature after gating is passed directly to the classifier. In the Quantum mode, the same latent feature is processed by the QEP, which generates observable-based quantum statistics, classically decodes them into the shared latent space, and adaptively fuses them with the original classical representation. This comparison isolates the representational contribution of the quantum-enhanced branch under otherwise matched training conditions.

We evaluate both inference performance and internal QEP behavior. Inference is reported under both the standard decision threshold and a validation-optimized threshold derived from Youden’s J statistic and applied to the test split. Internal analysis tracks the mean fusion coefficient α , the dispersion of the quantum-enhanced branch through q -std, and their joint behavior across training. This design allows us to assess not only whether the QEP changes output metrics, but also how its internal operating regime depends on the tensor-network frontend.

To further characterize the behavior of the QEP in the most favorable frontend setting observed in Experiment 1, we additionally analyze the TTN-based model with respect to qubit scaling and noise sensitivity. For qubit scaling, the QEP is instantiated with $N_q \in \{4, 6, 8, 10, 12, 14, 16\}$, and the resulting test-accuracy distributions are compared against the classical TTN baseline. For noise sensitivity, we fix $N_q = 8$

TABLE I: Scenario definitions for the MPC benchmark.

Scenario	Definition
0	Insecure baseline
1	Passive, aggregation only
2	Passive, aggregation + normalization
3	Passive, aggregation + normalization + transformation
4	Active, aggregation only
5	Active, aggregation + normalization
6	Active, aggregation + normalization + transformation

and compare the classical TTN baseline with four quantum execution conditions: noiseless, depolarizing, thermal, and mixed noise. Both analyses are reported as distributional summaries of test accuracy over repeated runs, allowing comparison of both central tendency and variability across conditions.

B. Experiment 2: MPC Mode Benchmark

The second experiment benchmarks the communication cost of MPC-secured aggregation under progressively stronger protection settings. The benchmark isolates the server-side communication induced by protected latent aggregation and is therefore not intended as a full accounting of all end-to-end distributed traffic. Rather, it provides a controlled analysis of how protected latent dimension and security setting determine the communication burden of the secure aggregation stage itself.

We vary the number of clients from $n = 1$ to 30. For each value of n , we consider seven scenarios. Scenario 0 is an insecure baseline in which a central server S performs the post-client aggregation and transformation directly. Scenarios 1–3 correspond to passive-security MPC settings with progressively richer protected functionality: Scenario 1 protects only weighted aggregation, Scenario 2 additionally protects normalization, and Scenario 3 further protects the post-aggregation transformation stage. Scenarios 4–6 are the corresponding active-security counterparts. Table I summarizes the security setting and protected functionality associated with each scenario.

1) *Cost Model and Measurement Protocol*: We employ a symbolic cost meter to quantify the communication cost of each scenario. The meter tracks three types of communication: (i) data sent by clients to computation nodes, (ii) data exchanged between computation nodes, and (iii) data transmitted during output reconstruction.

In all scenarios, we assume $k = 64$, corresponding to an encoding in which client inputs fit into 64-bit machine words. For Scenarios 2 and 5, division is metered using $\theta = 5$. This benchmark is intended to capture relative scaling trends across MPC scenarios rather than protocol-tight cryptographic cost bounds. Additional implementation overheads that may arise in practice are not included in the present cost model.

2) *Fairness and Comparability Across Modes*: To avoid conflating security modeling with numerical instability, we assume that fixed-point parameters can be chosen so that the accuracy of the MPC computation matches that of the original insecure floating-point computation. As noted in [37],

automated tools can assist in fixed-point parameter selection. Under this assumption, the benchmark should be interpreted as a comparison of secure-computation overheads under matched numerical behavior, rather than as a study of accuracy degradation caused by quantization or approximation artifacts.

V. RESULTS AND ANALYSIS

A. Results of Experiment 1: Quantum Enhancement across MPS, TTN, and MERA

Fig. 4 and 5 summarize the inference performance and internal QEP behavior in the comparison between Classical and Quantum modes across MPS, TTN, and MERA. Overall, the results indicate that the effect of quantum enhancement is architecture-dependent rather than uniform across tensor-network frontends.

Under threshold-optimized evaluation, the combination of tensor-network architecture and post-aggregation quantum enhancement clearly affects the performance profile. The main effect of the QEP is not a uniform increase in overall Accuracy, but a redistribution of class-wise Precision, Recall, and F1 across frontend types. In the present study, TTN exhibits the most balanced overall profile, achieving strong Accuracy and Pneumonia F1 while remaining competitive on the remaining class-wise metrics. MPS and MERA also remain competitive, but their gains under quantum enhancement are less consistently aligned with the strongest downstream performance.

From a clinical perspective, an important observation is that Pneumonia Recall remains high across all architectures, at around 0.90. This suggests that the proposed hybrid pipeline maintains strong sensitivity to positive cases even when the frontend architecture changes. In screening-oriented settings, where missed pneumonia cases are often more critical than moderate changes in aggregate balanced metrics, this is an encouraging property of the overall framework.

The internal diagnostics further show that the QEP operates differently depending on the frontend. Although the mean fusion coefficient α decreases over training for all three architectures, the resulting operating regimes differ substantially. MPS reaches the highest final q -std, MERA remains intermediate, and TTN stabilizes at a comparatively lower and more controlled quantum-branch dispersion. This indicates that the effect of the QEP is not explained by quantum-branch variability alone. Instead, the results suggest that learning performance is shaped by the interaction between frontend topology and post-aggregation quantum refinement, with TTN providing the most favorable balance in the present setting.

Fig. 6 summarizes additional analyses for the TTN-based QEP, focusing on qubit-count scaling and noise robustness. Because TTN provides the most favorable overall profile in the frontend comparison, we use it here as the reference setting for a more detailed examination of the operating range of the quantum branch.

The left panel shows the test-accuracy distributions of the TTN+QEP model for qubit counts from 4 to 16, together with the classical TTN baseline. The lower-qubit settings, especially $N_q = 4$ and $N_q = 6$, tend to show lower or less

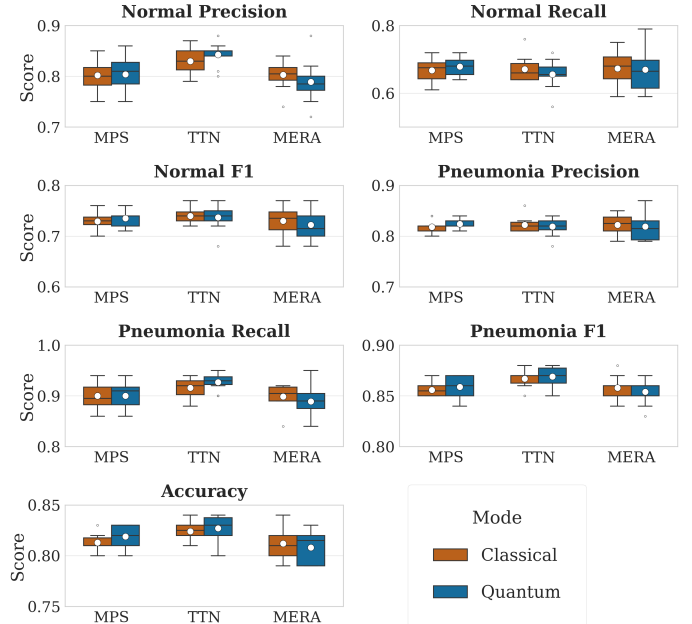


Fig. 4: Threshold-optimized test performance of the Classical and Quantum modes across MPS, TTN, and MERA. Boxplots report class-wise Precision, Recall, F1-score, and overall Accuracy. Results are shown for the default QEP setting ($N_q = 16$).

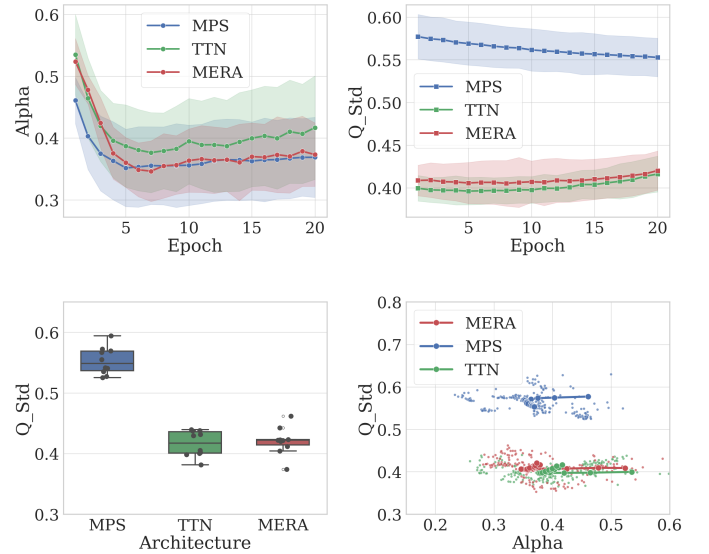
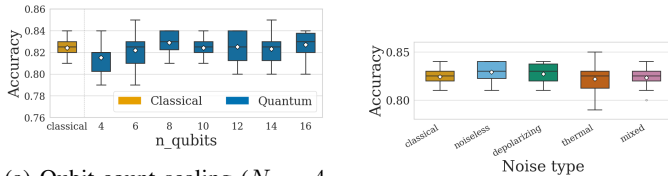


Fig. 5: Internal behavior of the QEP across MPS, TTN, and MERA: (A) evolution of α , (B) evolution of q -std, (C) final-epoch q -std distribution, and (D) α - q -std phase behavior.

favorable accuracy distributions than the higher-qubit settings. By contrast, from $N_q \geq 8$, the distributions appear more stable and remain within a broadly similar range. In the present TTN-based setting, this suggests that the QEP operates more reliably once the qubit count is sufficiently matched to the 64-dimensional latent representation.

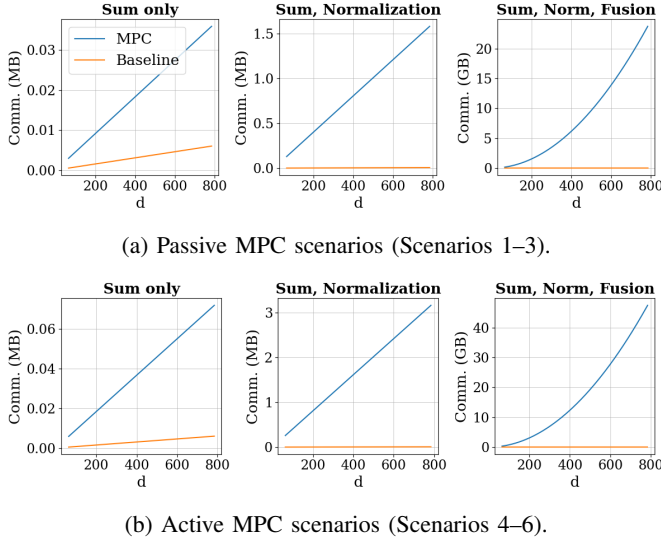
The right panel shows the test-accuracy distributions for the



(a) Qubit-count scaling ($N_q = 4$ to 16).

(b) Noise robustness at $N_q = 8$.

Fig. 6: TTN-based Quantum-Enhanced Processor (QEP): (a) test-accuracy distributions under qubit-count scaling ($N_q = 4$ to 16), and (b) robustness under representative noise conditions at $N_q = 8$. The classical TTN baseline is included for reference.



(a) Passive MPC scenarios (Scenarios 1–3).

(b) Active MPC scenarios (Scenarios 4–6).

Fig. 7: Modeled communication overhead as a function of protected representation dimension for passive and active MPC scenarios.

TTN+QEP model at $N_q = 8$ under different noise conditions. Relative to the noiseless setting, all noisy conditions exhibit some degree of performance degradation, although the extent of degradation varies across noise types. The depolarizing setting remains comparatively close to the noiseless case, whereas the thermal setting shows a wider spread and includes lower-performing runs, indicating stronger sensitivity under that noise model. The mixed-noise setting also shows a degradation trend relative to the noiseless setting while retaining a broadly comparable overall range. Taken together, these results suggest that the TTN-based QEP is affected by noise in a noise-type-dependent manner.

B. Results of Experiment 2: MPC Benchmark

Fig. 7a and 7b summarize the modeled communication overhead for the passive and active MPC scenarios, together with the insecure baseline.

The results show that, under the present abstraction of server-side MPC communication, the dominant communication cost is governed by the bit-width k , the protected

representation dimension, and the selected protection scenario, rather than by the number of aggregated clients itself. Because the benchmark isolates the communication induced by MPC processing of protected latent representations, client count does not appear as the dominant scaling factor in the present formulation. In both figures, $k = 64$ is fixed while the protected representation dimension varies from the raw dimension $D_{\text{raw}} = 784$ to the compressed latent dimension $d = 64$.

a) Active versus passive security.: Active security preserves the same qualitative scaling trend as passive security while introducing a moderate multiplicative overhead. In the present protocol model, this additional cost is limited, although different protocol assumptions could lead to substantially larger overheads.

b) Effect of representation compression.: The dominant communication trend is governed by the representation dimension. This indicates that client-side compression has a direct impact on the effective cost of secure aggregation: reducing the latent dimension before MPC reduces the communication surface on which security overhead is applied.

c) Varying the number of clients.: Because the present benchmark isolates the communication cost of the MPC stage itself, the number of clients does not emerge as the dominant scaling factor in the reported curves. This is also true for the insecure baseline when only the output-side aggregation communication is considered. Even if client-to-aggregator transmission were explicitly included, the main conclusion would remain unchanged: under the linear secret-sharing model considered here, the dominant cost trend is governed primarily by the protected representation dimension and the protection scenario rather than by the number of aggregated clients.

VI. DISCUSSION

The results of Experiment 1 suggest that the QEP should be understood not as a universal accuracy booster, but as a quantum feature-refinement mechanism whose effectiveness depends on how it is paired with the tensor-network frontend. Across MPS, TTN, and MERA, the QEP does not yield a uniform increase in Accuracy or F1-score. Instead, its contribution appears through architecture-dependent changes in class-wise operating characteristics and in the internal fusion dynamics of the model. The main implication is therefore not the superiority of any single component in isolation, but the importance of jointly designing tensor-network structure and post-aggregation quantum refinement.

Within this broader picture, TTN exhibits the most favorable overall profile in the present setting. It achieves strong predictive performance, including high Accuracy and Pneumonia F1, while maintaining high sensitivity to pneumonia-positive cases. More importantly, however, the results indicate that the contribution of the QEP is conditioned by the latent representation supplied by the frontend. MPS, TTN, and MERA do not merely compress the input differently; they expose different latent organizations to the QEP, which in turn leads to different quantum operating regimes.

The internal diagnostics support this interpretation. MPS exhibits the largest quantum-branch dispersion, whereas TTN remains in a lower and more controlled q -std regime. This suggests that larger internal quantum variability does not automatically translate into stronger downstream performance. In the present experiment, the most favorable learning behavior emerges not from the largest quantum-branch spread, but from a more balanced interaction between quantum refinement and the frontend-induced latent structure. From a quantum-machine-learning perspective, this indicates that the effect of post-aggregation quantum enhancement is jointly determined by the quantum map and the representational topology that feeds it.

The qubit-scaling and noise analyses provide an additional practical perspective on the TTN-based QEP. For the present 64-dimensional latent input, lower-qubit configurations, particularly $N_q = 4$ and $N_q = 6$, appear to provide insufficient feature capacity, whereas the behavior becomes more stable from $N_q = 8$ onward. In addition, all noisy conditions at $N_q = 8$ show some degree of degradation relative to the noiseless case, although the extent of degradation depends on the noise model. These observations do not establish hardware scalability, but they indicate that, in the TTN setting, the hybrid pipeline retains meaningful operating behavior once the quantum register size is reasonably matched to the latent dimension.

From a clinical perspective, the consistently high Pneumonia Recall across architectures is encouraging. In screening or triage settings, sensitivity to pneumonia-positive cases is often more important than small fluctuations in class-balanced aggregate metrics, because false negatives carry disproportionate clinical cost. The present results therefore suggest that hybrid TN+QEP pipelines can preserve clinically relevant sensitivity while still allowing architectural differences to shape the overall operating point.

Experiment 2 complements this interpretation from the systems side. Because the communication cost is dominated by the protected representation dimension, tensor-network compression directly reduces the communication overhead incurred by MPC on that representation. Thus, the framework not only shapes the latent interface for the QEP, but also improves the practical outlook for privacy-preserving deployment by lowering the effective cost of secure aggregation.

At the same time, the present study has several limitations. First, the quantum branch is evaluated through Qiskit Aer statevector simulation, so the results should be interpreted as evidence for hybrid representational behavior rather than as a demonstration of hardware-level feasibility. Moreover, the present study does not establish that the quantities computed by the QEP are classically intractable or impractical to obtain classically. Rather, the QEP is used here as a structured small-qubit feature map, and the focus is on its representational interaction with tensor-network-compressed latent features rather than on computational advantage. Second, the current comparison does not yet isolate which portion of the observed QEP effect is uniquely attributable to the quantum observable

map itself, as opposed to the broader effect of introducing an additional nonlinear transformation pathway. Third, the MPC benchmark is based on symbolic communication-cost modeling and therefore does not replace full protocol-level implementation and empirical measurement.

VII. CONCLUSION

In this work, we investigated the role of the QEP within a privacy-aware federated learning framework for medical image classification. The proposed architecture combines client-side tensor-network representation learning, an abstract secure-aggregation model for MPC benchmarking, and a post-aggregation quantum refinement module based on observable expectation values, classical decoding, differentiable bypass fusion, and adaptive residual mixing.

Our results show that the contribution of the QEP is strongly architecture-dependent. Rather than acting as a uniform accuracy amplifier, the QEP reshapes inference behavior in a manner determined by its interaction with the tensor-network frontend. In the present setting, TTN exhibits the most favorable overall profile, while MPS, TTN, and MERA occupy distinct operating regimes in the joint behavior of fusion dynamics and quantum-branch dispersion. The broader conclusion is therefore that learning performance is governed not by the quantum module alone, but by the co-design of tensor-network structure and post-aggregation quantum refinement.

The additional qubit-scaling and noise analyses further clarify the practical behavior of the QEP. For the present 64-dimensional latent input, performance becomes more stable from 8 qubits onward, while noisy conditions at 8 qubits degrade performance relative to the noiseless case in a noise-type-dependent manner. These results do not establish hardware-level benefit, but they help characterize the operating range and robustness of the hybrid quantum branch within the proposed pipeline.

From the systems perspective, the MPC benchmark shows that the dominant communication factor is the size of the protected latent representation. This highlights a second contribution of the architecture: tensor-network compression not only shapes the latent space on which quantum refinement operates, but also reduces the communication overhead to which secure computation is applied. Overall, the results support a co-design view of privacy-aware hybrid medical AI in which representation compression, post-aggregation quantum refinement, and secure deployment should be optimized jointly rather than treated as isolated components.

While the present results are obtained in a simulator-based regime, an important motivation of the proposed framework lies in future hardware-oriented use beyond the classically simulable range. When quantum processors with on the order of tens of usable qubits are employed in regimes where full classical simulation is no longer practical, it becomes meaningful to apply quantum processing to tensor-network-compressed latent features rather than to the original large-scale input. In this sense, compressing very high-dimensional data—for example, from hundreds of thousands of dimensions

to a few hundred latent features—may provide a realistic pathway for practical quantum-enhanced learning on future devices.

Future work will proceed in three directions. First, implementing end-to-end cryptographic MPC with explicit fixed-point execution will allow direct validation of the present cost model and a more detailed characterization of secure learning performance. Second, protocol-level optimization will be necessary to improve scalability and reduce the overhead of stronger security scenarios. Third, further study of the QEP—including deeper circuits, stronger ablation against capacity-matched classical surrogates, and more realistic noisy or hardware-backed settings—will be important for clarifying when hybrid quantum enhancement provides meaningful benefit in privacy-aware federated learning.

ACKNOWLEDGMENTS

The authors acknowledge helpful conversations with Mark Medum Bundgaard, Miyoji Kakinuki, Akiko Kamigori, Kazufumi Okazaki, Tomah Sogabe, Naoki Yamamoto, Eriko Kaminishi, Toshiki Yasuda. Hiroshi Yamauchi acknowledges the support of Yoshi-aki Shimada, Yosuke Komiyama and Ryuji Wakikawa. This work was partly supported by NEDO Challenge Quantum Computing “Solve Social Issues!”.

REFERENCES

- [1] N. Rieke, J. Hancox, W. Li, F. Milletari, H. R. Roth, and et al., “The future of digital health with federated learning,” *npj Digital Medicine*, vol. 3, no. 119, 2020.
- [2] M. J. Sheller, G. A. Reina, B. Edwards, J. Martin, and S. Bakas, “Federated learning in medicine: Facilitating multi-institutional collaborations without sharing patient data,” *Scientific Reports*, vol. 10, no. 12598, 2020.
- [3] European Parliament and Council, “Regulation (eu) 2016/679 (general data protection regulation),” 2016, official Journal of the European Union.
- [4] U.S. Congress, “Health insurance portability and accountability act of 1996,” 1996.
- [5] Government of Japan, “Act on the protection of personal information (japan),” 2003, amended 2022.
- [6] —, “Act on anonymized medical data that are meant to contribute to research and development in the medical field,” 2017, act No. 28 of 2017.
- [7] European Commission, “Proposal for a regulation on the european health data space,” 2022, cOM(2022) 197 final.
- [8] B. McMahan, E. Moore, D. Ramage, S. Hampson, and B. A. y Arcas, “Communication-efficient learning of deep networks from decentralized data,” *Proceedings of AISTATS*, 2017.
- [9] P. Kairouz and et al., “Advances and open problems in federated learning,” *Foundations and Trends in Machine Learning*, vol. 14, no. 1-2, pp. 1–210, 2021.
- [10] L. Zhu, Z. Liu, and S. Han, “Deep leakage from gradients,” in *NeurIPS*, 2019.
- [11] R. Shokri, M. Stronati, C. Song, and V. Shmatikov, “Membership inference attacks against machine learning models,” in *IEEE S&P*, 2017.
- [12] K. Bonawitz and et al., “Practical secure aggregation for privacy-preserving machine learning,” in *Proceedings of CCS*, 2017.
- [13] A. Broadbent, J. Fitzsimons, and E. Kashefi, “Universal blind quantum computation,” in *Proceedings of the 50th Annual IEEE Symposium on Foundations of Computer Science (FOCS 2009)*, 2009, pp. 517–526.
- [14] J. F. Fitzsimons, “Private quantum computation: an introduction to blind quantum computing and related protocols,” *npj Quantum Information*, vol. 3, p. 23, 2017.
- [15] Y. Ma, E. Kashefi, M. Arapinis, K. Chakraborty, and M. Kaplan, “Qenclave - a practical solution for secure quantum cloud computing,” *npj Quantum Information*, vol. 8, p. 128, 2022.

- [16] L. Pira and C. Ferrie, “An invitation to distributed quantum neural networks,” *Quantum Machine Intelligence*, vol. 5, p. 23, 2023.
- [17] H. Tang, B. Li, G. Wang, H. Xu, C. Li, A. Barr, P. Cappellaro, and J. Li, “Communication-efficient quantum algorithm for distributed machine learning,” *Physical Review Letters*, vol. 130, p. 150602, 2023.
- [18] D. Barral, F. J. Cardama, G. Díaz-Camacho, D. Failde, I. F. Llovo, M. Miras-Suárez, J. Vázquez-Pérez, J. Villaluso, C. Piñeiro, N. Costas, J. C. Piel, T. F. Pena, and A. Gómez, “Review of distributed quantum computing: From single qpu to high performance quantum computing,” *Computer Science Review*, vol. 57, p. 100747, 2025.
- [19] D. Ferrari and M. Amoretti, “A design framework for the simulation of distributed quantum computing,” in *Proceedings of the 2024 Workshop on High Performance and Quantum Computing Integration*, ser. HPCQI '24, 2024, pp. 4–10.
- [20] S. Y.-C. Chen, C.-M. Huang, C.-W. Hsing, and Y.-J. Kao, “Hybrid quantum-classical classifier based on tensor network and variational quantum circuit,” *arXiv:2011.14651*, 2020.
- [21] X.-Z. Luo, Z. Li, and J. Li, “Quantum simulation with hybrid tensor networks,” *arXiv:2007.00958*, 2020.
- [22] N. Tornow, C. B. Mendl, and P. Bhatotia, “Quantum-classical computing via tensor networks,” *arXiv:2410.15080*, 2024.
- [23] Y. Chen, C.-Y. Kuo, Y. Du, D. Tao, and X. Wu, “Ted-q: a tensor network enhanced distributed hybrid quantum machine learning framework,” *arXiv:2301.05451*, 2023.
- [24] C.-Y. Liu, C.-H. A. Lin, and K.-C. Chen, “Quantum-train with tensor network mapping model and distributed circuit ansatz,” in *ICASSP 2025*. IEEE, 2025.
- [25] A. Ternovaya, A. Melnikov, V. Mamenchikov, N. Belokonev, S. Dolgov, A. Berezutskii, R. Ellerbrock, A. Mansell, and M. Perelshtein, “Tensor quantum programming,” *arXiv:2403.13486*, 2024.
- [26] C. Li, N. Kumar, Z. Song, S. Chakrabarti, and M. Pistoia, “Privacy-preserving quantum federated learning via gradient hiding,” *Quantum Science and Technology*, vol. 9, no. 3, 2024.
- [27] A. Kardashin, A. Uvarov, and J. Biamonte, “Quantum machine learning tensor network states,” *Frontiers in Physics*, vol. 8, 2020.
- [28] A. Obukhov, M. Rakhuba, A. Liniger, Z. Huang, S. Georgoulis, D. Dai, and L. Van Gool, “Spectral tensor train parameterization of deep learning layers,” in *Proceedings of The 24th International Conference on Artificial Intelligence and Statistics*, ser. Proceedings of Machine Learning Research, vol. 130, 2021, pp. 3547–3555.
- [29] Y. Chen, Y. Pan, and D. Dong, “Residual tensor train: A quantum-inspired approach for learning multiple multilinear correlations,” *IEEE Transactions on Artificial Intelligence*, vol. 4, pp. 1101–1113, Oct. 2023.
- [30] J. Dborin, F. Barratt, V. Wimalaweera, L. Wright, and A. G. Green, “Matrix product state pre-training for quantum machine learning,” *Quantum Science and Technology*, vol. 7, no. 3, p. 035014, 2022.
- [31] A. Mossi, B. Žunković, and K. Flouris, “A matrix product state model for simultaneous classification and generation,” *Quantum Machine Intelligence*, vol. 7, 2025.
- [32] J. Y. Araz and M. Spannowsky, “Quantum-inspired event reconstruction with tensor networks: Matrix product states,” *Journal of High Energy Physics*, no. 08, p. 112, 2021.
- [33] Y. Zhao and T. Cui, “Tensor-train methods for sequential state and parameter learning in state-space models,” *Journal of Machine Learning Research*, vol. 25, pp. 1–51, 2024.
- [34] X. Zhang, E. Kofidis, C. Zhu, L. Zhang, and Y. Liu, “Federated learning using coupled tensor train decomposition,” *arXiv:2403.02898*, 2024.
- [35] A. S. Bhatia and D. E. Bernal Neira, “Federated hierarchical tensor networks: A collaborative learning quantum ai-driven framework for healthcare,” *arXiv:2405.07735*, 2024.
- [36] J. Yang et al., “Medmnist v2: A large-scale lightweight benchmark for 2d and 3d biomedical image classification,” *Scientific Data*, 2023.
- [37] D. Rathee, M. Rathee, R. K. K. Goli, D. Gupta, R. Sharma, N. Chandran, and A. Rastogi, “Sirnn: A math library for secure RNN inference,” in *42nd IEEE Symposium on Security and Privacy, SP 2021, San Francisco, CA, USA, 24-27 May 2021*. IEEE, 2021, pp. 1003–1020.